Electronic Supplementary Information

Human Skin-Inspired Integrated Multidimensional Sensors Based on Highly Anisotropic Structures

Haomin Chen,[a, b] Ying Jing,[c] Jeng-Hun Lee,[a] Dan Liu,[a] Jungmo Kim,[b] Shusheng Chen,[a] Kan Huang,[c] Xi Shen,[a] Qingbin Zheng,[a] Jinglei Yang,[a]* Seokwoo Jeon,[b]* and Jang-Kyo Kim[a]**

[a] Department of Mechanical and Aerospace Engineering, The Hong Kong University of Science and Technology, Clear Water Bay, Kowloon, Hong Kong

E-mail: zhengqingbin@cuhk.edu.cn (Q.B. Zheng); maeyang@ust.hk (J.L. Yang); mejkkim@ust.hk (J.K. Kim)

[b] Department of Material Science and Engineering, KAIST Institute for The Nanocentury, Korea Advanced Institute of Science and Technology, Daejeon 305-701, Republic of Korea.

E-mail: jeon39@kaist.ac.kr (S. Jeon)

[c] Department of Electronic and Computer Engineering, The Hong Kong University of Science and Technology, Clear Water Bay, Kowloon, Hong Kong

Experimental Section

Fabrication of PUGA/PDMS in-plane sensors: GO sheets were exfoliated from natural graphite flakes (supplied by Asbury Graphite Mills) using the modified Hummers method[1, 2] and dispersed in deionized water. Highly aligned GO aerogels were prepared by unidirectional freeze-casting of the GO aqueous dispersion (5 mg ml^{-1}) using liquid nitrogen as the cooling source (Figure S1a). Briefly, GO dispersion was poured into a plastic mold with an aluminum bottom plate. The mold was placed on a metal scaffold immersed in liquid nitrogen to generate

a large temperature gradient between the bottom and top of dispersion. The temperature gradient forced the ice to grow vertically and thus the alignment of GO sheets along the ice growth direction.[3-6] It should be noted that the side wall of mold was wrapped with polystyrene foam for thermal insulation so as to avoid undesirable alignment in the horizontal direction. The GO aerogel was obtained after freeze-drying in a freeze-dryer (Model: SCIENTZ-10N) at -50 ℃ and 10 Pa for 48 h. The GO aerogels were stabilized in air at 200 ℃ for 2 h and reduced in argon at 900 ℃ for 2 h to obtain UGAs. In order to enhance the anisotropic piezoresistive properties, the UGA was biaxially compressed along two orthogonal axes transverse to graphene alignment to generate pre-cracks. Specifically, the UGA was first compressed at 90 % strain along one axis, and then further compressed in the orthogonal axis under the same strain. Different pre-strains were used to control the anisotropic electrical responses of PUGAs. The orthogonal compressions were released after 30 sec to allow the recovery of porous structures in PUGAs. The PUGAs were infiltrated with PDMS (Sylgard 184, Dow Corning, at a base to curing agent weight ratio of 10:1) assisted by vacuum and heated at 80 ℃ for 2 h for complete curing. The PUGA/PDMS composites were cut along the alignment direction into thin films. It is known that sensing performance can be adjusted by the dimensions of sensing films.[7, 8] Here the dimensions of composite films were fixed at 25 mm long × 4 mm wide × 0.5 mm thick to achieve comparable stretchability to human skin. The composite films were placed on a PDMS substrate to form a composite film. EGaIn (≥ 99.99 % trace metals basis supplied by Aldrich) was applied to two ends of the composite film to connect copper wires, and another layer of PDMS was applied on top to protect the connection sites.

Fabrication of patterned Au/PDMS pressure sensor and integration of multidimensional sensors: PS spheres with different sizes were first synthesized through dispersion polymerization.[9] Highly ordered PS sphere monolayer arrays were prepared by spin-coating of PS suspension onto pre-treated glass slides.[10] The PDMS films with concave morphologies were then molded using the PS sphere array template. After removing the remnant spheres with

acetone, the film was dried and coated with a thin layer of Au to facilitate the separation between PDMS. The prepolymer of stiff PDMS at a base to curing agent weight ratio of 2:1 was cast onto the negative mold and cured to obtain the thin film with a convex microdome pattern. Patterned PDMS with a feature size of 1.6 μm was chosen to construct the pressure sensor with high pressure sensitivity. A 50 nm layer of Au nanoparticles was sputtered onto the patterned surface as conductive fillers. The patterned Au/PDMS composites were cut into 10 mm squares of 0.5 mm in thickness and placed into the center of a 35 mm square mold. The gap was filled with soft PDMS, which was prepared by mixing the prepolymer PDMS (Silgard 184, at a base to curing agent ratio of 10:1 by weight) and the inhibitor (polyethylenimine, 80 % ethoxylated solution (35 % aqueous solution), M_w = 70,000) at a weight ratio of 100 to 0.3 to reduce the crosslinking densities.[11] The whole structure was cured at 60 ℃ for 2 h to achieve heterogeneous stiffnesses between the central patterned region and the surrounding region. The Au/PDMS film was connected to the copper wires at one end using silver paint. Two identical Au/PDMS films were then packaged face-to-face to obtain the pressure sensor. For the multidimensional sensor, one pressure sensor was further laminated with two PUGA/PDMS in-plane sensors using PDMS as adhesive to avoid any sliding at the interfaces.

Characterization: The morphologies of PUGA, PUGA/PDMS, and Au/PDMS composites were characterized using SEM (JEOL 6390F) and TEM (2010, JEOL). The X-ray photoelectron spectroscopy (XPS, Axis Ultra DLD) and X-ray diffraction (XRD) were used to study the elemental compositions and the crystal structures of GO and UGA. Partially recovered graphitic structures were observed from the TEM image of PUGA (Figure S1b). The deconvoluted XPS C1s spectrum of GO showed strong peaks of −COOH, C=O/C−O−C and −C−OH at ~289.1, 287.7 and 287.1 eV, respectively (Figure S1c). These peaks corresponding to oxygenated functional groups almost disappeared after reduction, leading to a surge of C/O atomic ratio from 1.8 in GO to 66.8 in UGA. The effectiveness of thermal reduction was further verified by XRD as shown in Figure S1d. The characteristic peak at 2θ = 10.3° corresponding to the (001)

plane indicates an interlayer spacing of 0.86 nm in GO. By contrast, a prominent (002) peak was observed at $2\theta = 25.6°$ in UGA corresponding to a d-spacing of 0.35 nm, consistent with the previous results.[12] To verify the anisotropic structure of PUGA quantitatively, fast Fourier transform (FFT) was performed on its SEM images taken from the alignment (Figure S1e and S1f) and transverse directions (Figure S1h and S1i) using ImageJ software. The angular dependence of pixel intensity in the FFT frequency domain images signifies the degree of the anisotropy.[13] The angular distributions of pixel intensity were fitted using the Cauchy-Lorentz distributions function (Figure S1g and S1j, respectively).[13, 14]

$$y = y_0 + \frac{2A}{\pi}\left(\frac{w}{4(x - x_0)^2 + w^2}\right) \quad \text{(S1)}$$

where x_0 represents the angle where the peak of the distribution locates, and w specifies the half-width at half-maximum (HWHM) value, indicating the degree of deviation from the principal orientation. The w value of PUGA in the alignment direction was 70, reflecting a well-aligned structure. In contrast, the same in the transverse direction was significantly higher, 2175, proving the highly anisotropic structure of PUGA.

The piezoresistive responses were measured by a digital multimeter (34970A Data Acquisition/Data Logger Switch Unit, Agilent). The average GFs of sensors were obtained from the measurements of more than five samples A universal testing machine (MTS Alliane RT-5) was used to apply in-plane uniaxial tension and normal pressure to the sensor. The local strains of the central stiff sections in the patterned Au/PDMS pressure sensor under uniaxial tension was measured by ImageJ from digital camera images.[15]

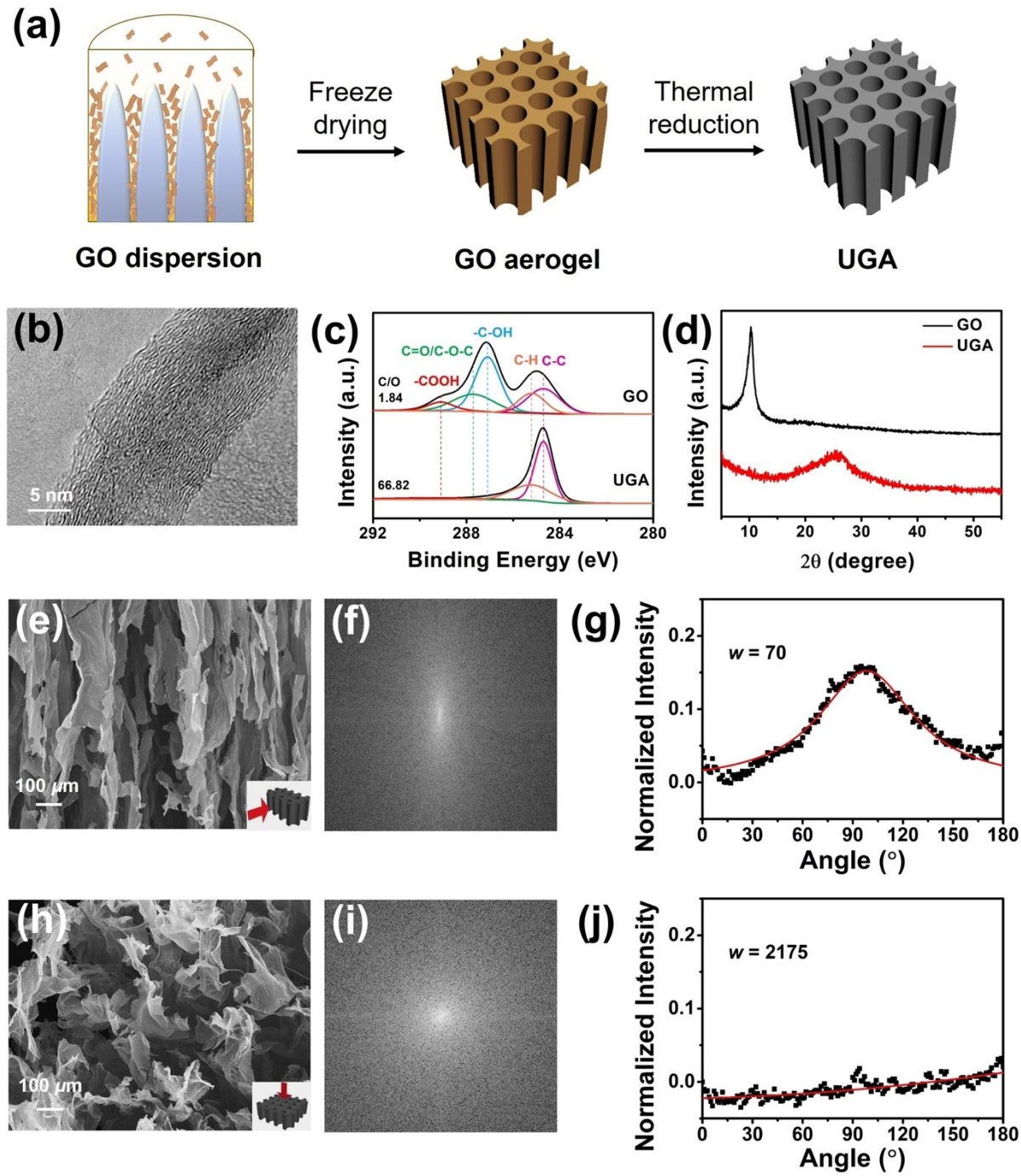

Figure S1. (a) Schematics of UGA fabrication. (b) High-resolution TEM image of graphene wall in PUGA; (c) XPS deconvoluted C1s and (d) general XRD spectra of GO and UGA; SEM images, corresponding FFT frequency domain images and angular analysis fitted with the Cauchy-Lorentz distribution function for PUGA taken from the (e-g) alignment and (h-j) transverse directions.

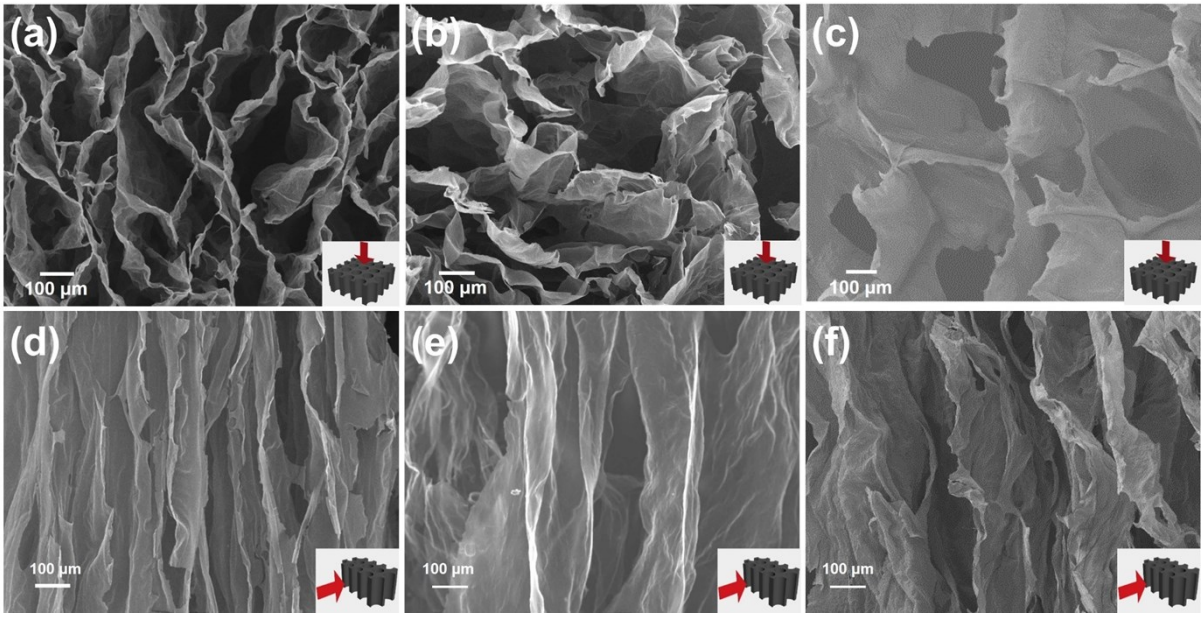

Figure S2. SEM images of UGAs freeze-cast at (a, d) -196 ℃, (b, e) -50 ℃, and (c, f) -20 ℃ showing the (a-c) top and (d-f) side views.

Freezing temperature plays an important role in controlling the aerogel structure.[16] Three different freezing temperatures, -20 ℃, -50 ℃ and -196 ℃, were used to obtain an optimal structure of UGAs. It is revealed that a lower freezing temperature gave rise to a larger number of transverse bridges connecting the graphene walls (Figure S2a-c). In addition, the UGAs prepared at -196 ℃ presented an average wall distance of only 62 ± 30 μm, which was much smaller than the aerogels frozen at -50 and -20 ℃ with wall distances of 161 ± 59 μm and 219 ± 72 μm, respectively (Figure S2d-f). Thus, -196 ℃ which produced aerogels with a dense porous structure was chosen for enhanced structural stability of UGAs.[3, 17]

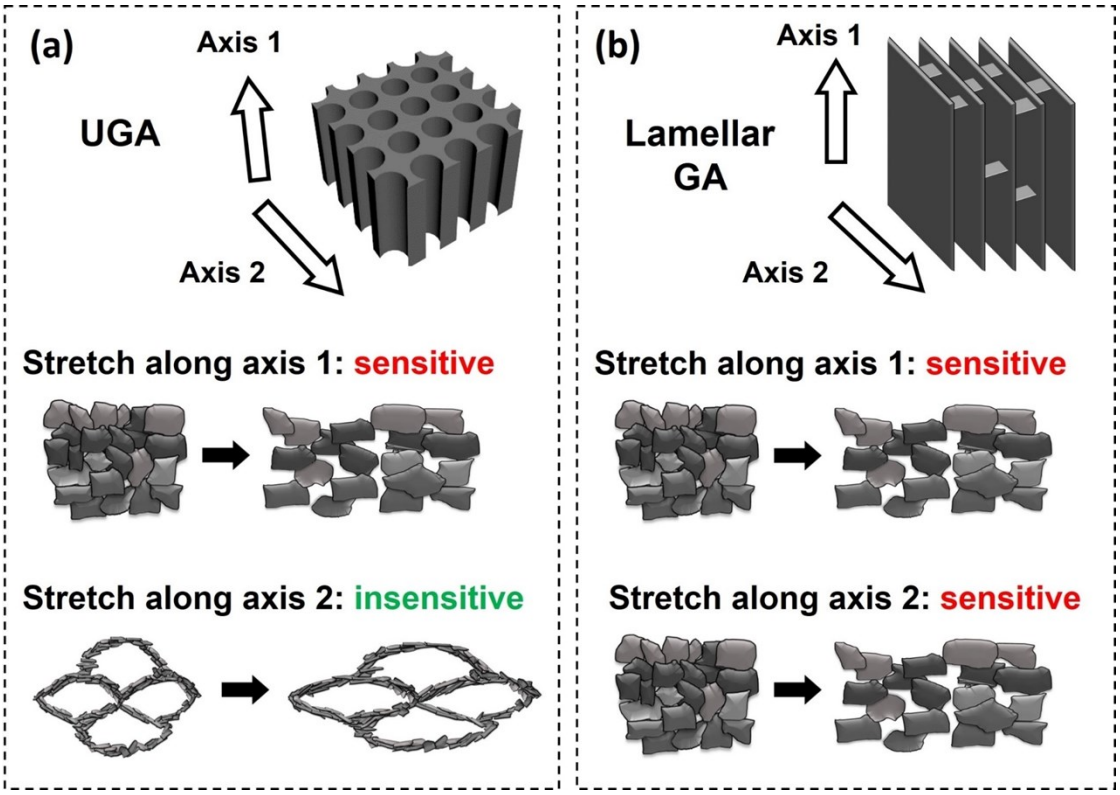

Figure S3. Schematics of sensing mechanisms based on the (a) UGA and (b) lamellar GA sensors when stretched along two orthogonal axes.

Unidirectional alignment is essential for 3D anisotropic piezoresistivity of the PUGA/PDMS strain sensor. If lamellar structures are used instead of the unidirectional structure,[18] the sensor would be sensitive to strains along the two alignment directions, which is undesirable for selective sensing capability.[19]

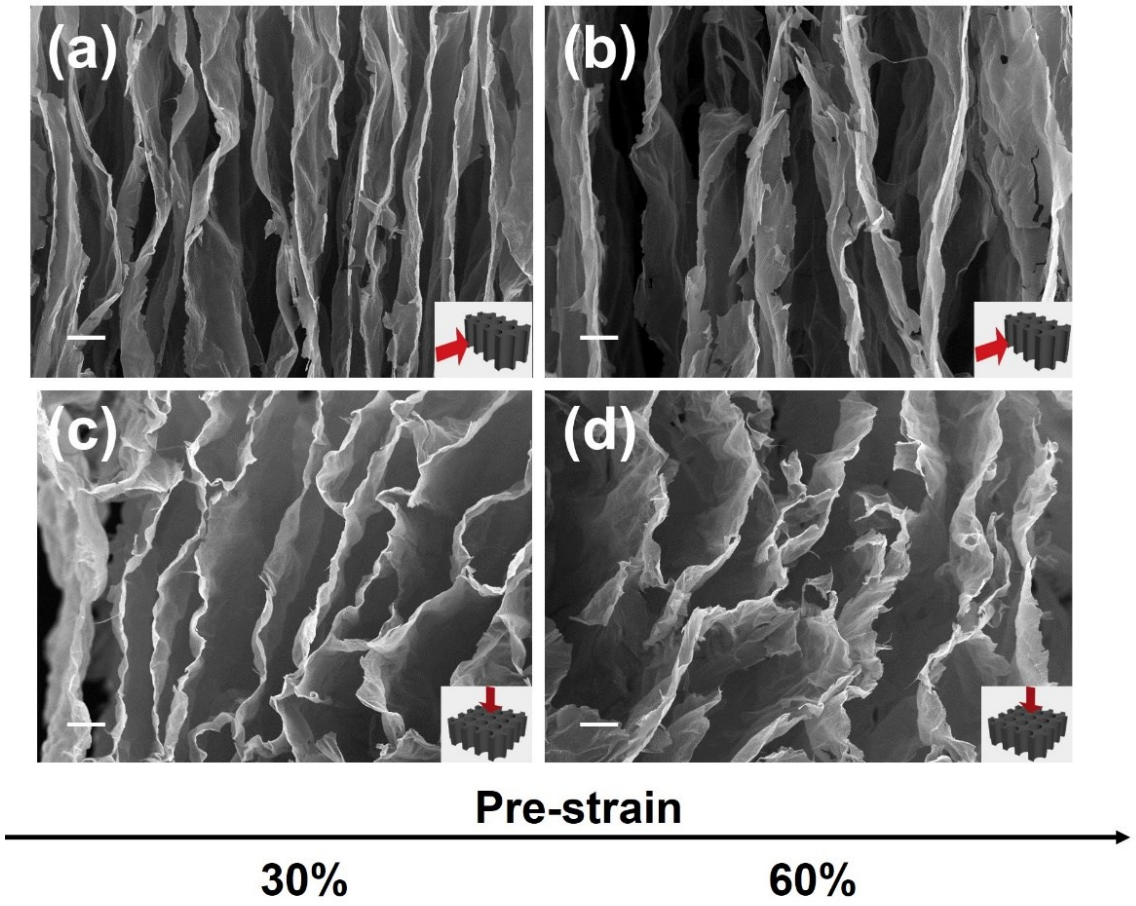

Figure S4. SEM images of PUGA in the (a, b) alignment and (c, d) transverse directions fabricated from (a, c) 30 % and (b, d) 60 % pre-strains. Scale bars are 100 μm.

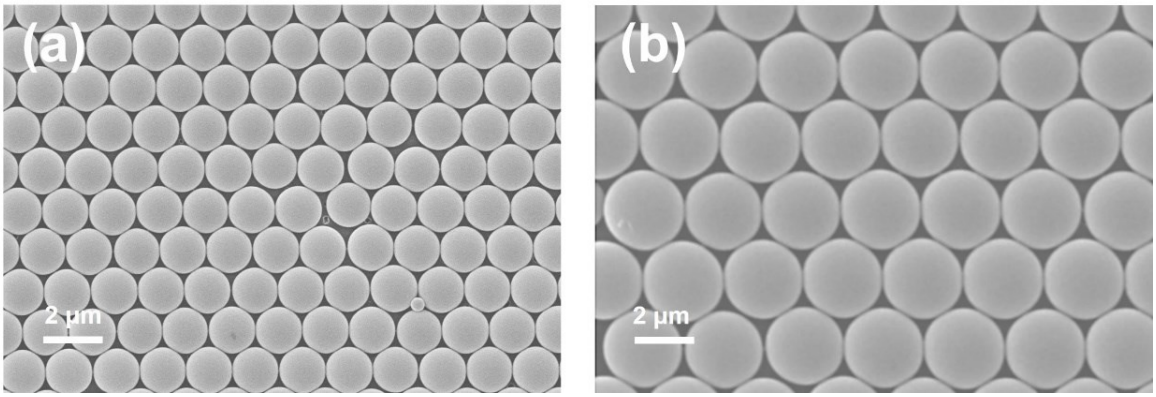

Figure S5. Hexagonal arrays of PS spheres of (a) ~1.6 μm and (b) ~2.6 μm in diameter.

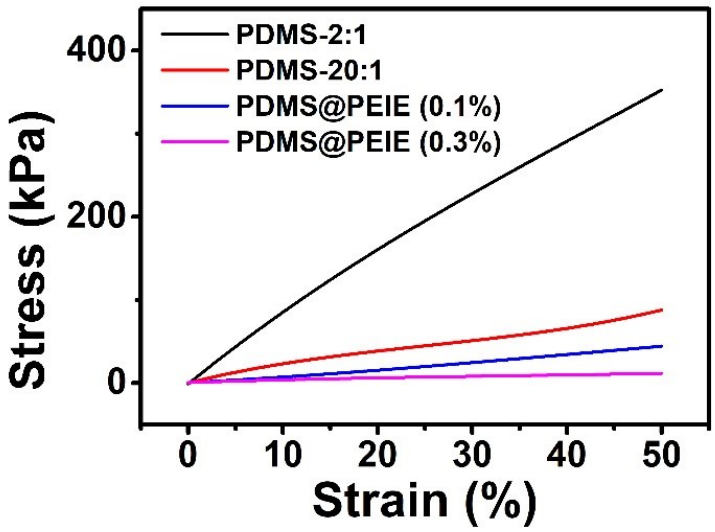

Figure S6. Tensile stress-strain curves of PDMS made from different components measured at a strain rate of 30 mm min^{-1}.

PDMS-2:1 and PDMS-20:1 were prepared by mixing base and curing agents at weight ratios of 2:1 and 20:1, respectively. A lower mixing ratio yielded stiffer PDMS due to a higher crosslinking density. 0.1 and 0.3 wt % of curing inhibitors, polyethyleneimine (PEIE), were mixed with the PDMS prepolymer at a base to curing agent weight ratio of 10:1 to prepare PDMS@PEIE (0.1 %) and PDMS@PEIE (0.3 %). PDMS-2:1 and PDMS@PEIE (0.3 %) were selected as the stiff and soft section of the stiffness gradient substrate, respectively, to generate a large modulus variation within the substrate.

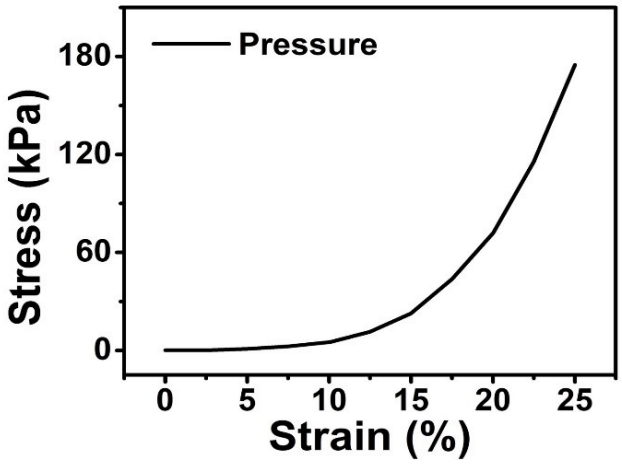

Figure S7. Stress-strain curve of PUGA/PDMS composite under uniaxial compression.

Table S1. Comparison of sensing performance with other 3D carbon structures at different strains.

Materials	GF at 5% strain	GF at 25% strain	Anisotropy	References
PUGA/PDMS	**26**	**196**	**Yes**	**This work**
Sliced graphene foam/PDMS	~13	~35	No	7
Graphene aerogel/PDMS	~50	NA	No	16
Graphene aerogel/natural rubber	~14	~34	No	20
3D-graphene films/PDMS	~16	~17	No	21
Bubble-derived graphene foam/PDMS	~5	~16	No	22
Printed graphene aerogel/PDMS	~2	~4	No	23
SWCNT/3D nanostructured PDMS	~25	~88	No	24
Anisotropic hybrid carbon aerogel/PDMS	~5	NA	Yes	25
Compressed graphene foam/PDMS	~10	~13	Yes	26

The PUGA/PDMS sensor in this work presented outstanding performance with higher GFs at both low (~5 %) and high strains (~25 %) than most of the other strain sensors based on 3D carbon structures, and unique anisotropic sensing behavior.[7, 16, 20-26] The high sensitivity throughout the wide sensing range comparable to the stretchability of human skin made it an enticing candidate for wearable applications involving low strains such as human-machine interfaces or high strains such as body motions monitoring.[27]

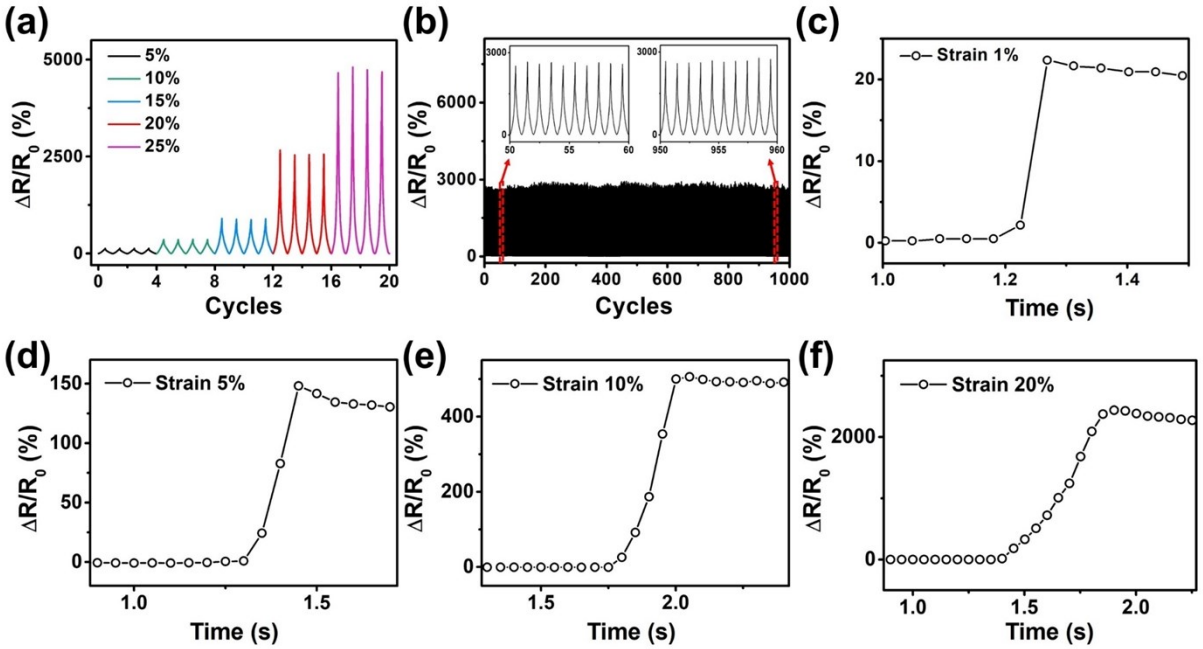

Figure S8. Relative resistance changes of PUGA/PDMS sensors under (a) cyclic tensile strains of 5 %, 10 %, 15 %, 20 % and 25 %, and (b) 1000 loading/unloading cycles at 20 % tensile strain; response times of PUGA/PDMS sensor under (c) 1 %, (d) 5 %, (e) 10 %, and (f) 20 % tensile strains.

Highly repeatable responses were observed under repeated loading/unloading cycles under different maximum strains (Figure S8a). To further characterize the reversibility and durability of the sensor, cyclic strains of different magnitudes were applied (Figure S8b). The rGO walls fractured upon stretching giving rise to a substantial increase in resistance, while the rGO sheets were drawn back to the initial condition with reconnected conductive paths by the flexible PDMS matrix upon release of applied strain, leading to reversible resistance responses. The resistance changes remained very stable and highly repeatable even after 1000 cycles at a maximum strain of 20 %, indicating excellent structural durability of the sensor. The good reversibility and durability can be attributed to the excellent flexibility of PDMS and its strong adhesion with rGO sheets.[28, 29] In addition, the sensor presented a short response time of less

than 78, 146, 252, and 452 ms for 1 %, 5 %, 10 % and 20 % strains at a strain rate of 10 mm s^{-1}, respectively. These values are comparable to those reported recently.[30-32] The quick response can be attributed to the stable conductive network and the flexibility of PDMS (Figure S8c-f).

Mechanism of Contact Resistance Changes in Interlocked Microdomes

The electrical current bundles together to pass through a multitude of discrete contact spots (a-spots) between the interlocked microdomes, leading to increased resistance.[33] The total resistance of the pressure sensor is mainly attributed to the contact resistance, which is composed of the self-resistance of contacted microdomes and the resistance caused by their mutual interactions. According to Holm's theory,[34, 35] the change in relative resistance can be written as:[36]

$$\frac{\Delta R}{R_0} = \frac{\sqrt{\frac{\pi\eta}{n_a}}\left(\frac{1}{\sqrt{A_{c,1}}} - \frac{1}{\sqrt{A_{c,0}}}\right)}{\sqrt{\frac{\pi\eta}{n_a A_{c,0}}} + \frac{1}{\alpha}} \quad \text{(S2)}$$

where n_a is the number of a-spots, α is the Holm radius referring to the radius of the a-spot cluster, $A_{c,1}$ and $A_{c,0}$ are the true contact area with and without external pressure, respectively. The true contact area between two microdomes is only a fraction of the apparent area (Figure S9a). Since α can be approximated as the radius of apparent contact area when there are a large number of a-spots at the contact interface,[33] the only variable causing resistance change is the true contact area.

Considering the hexagonal close packing arrangement, the total contact area of the interlocked array can be simplified as a sum of the contact area in each contacting units (Figure

S9b). Additionally, the number of a-spots can be estimated from the number of spheres of one patterned layer. Substituting $A_c = nA_{unit}$ and by $n_a = 3n$ into Equation S2 gives:

$$\frac{\Delta R}{R_0} = \frac{\frac{\sqrt{\pi\eta}}{n}\left(\frac{1}{\sqrt{3A_{unit,1}}} - \frac{1}{\sqrt{3A_{unit,0}}}\right)}{\frac{1}{n}\sqrt{\frac{\pi\eta}{3A_{unit,0}}} + \frac{1}{\alpha}} \quad \text{(S3)}$$

The finite element analysis (FEA) was performed to obtain the true contact area by simulating the deformation of interlocked microdomes under different pressures using a hyperelastic model (Figure S9c).[37] The relationship between $\Delta R/R_0$ and A in Equation S3 can be converted to the relationship between theoretical resistance change and external pressure based on the simulated result (Figure S9d). As shown in Figure S9e, the theoretical model agreed well with the experimental result.

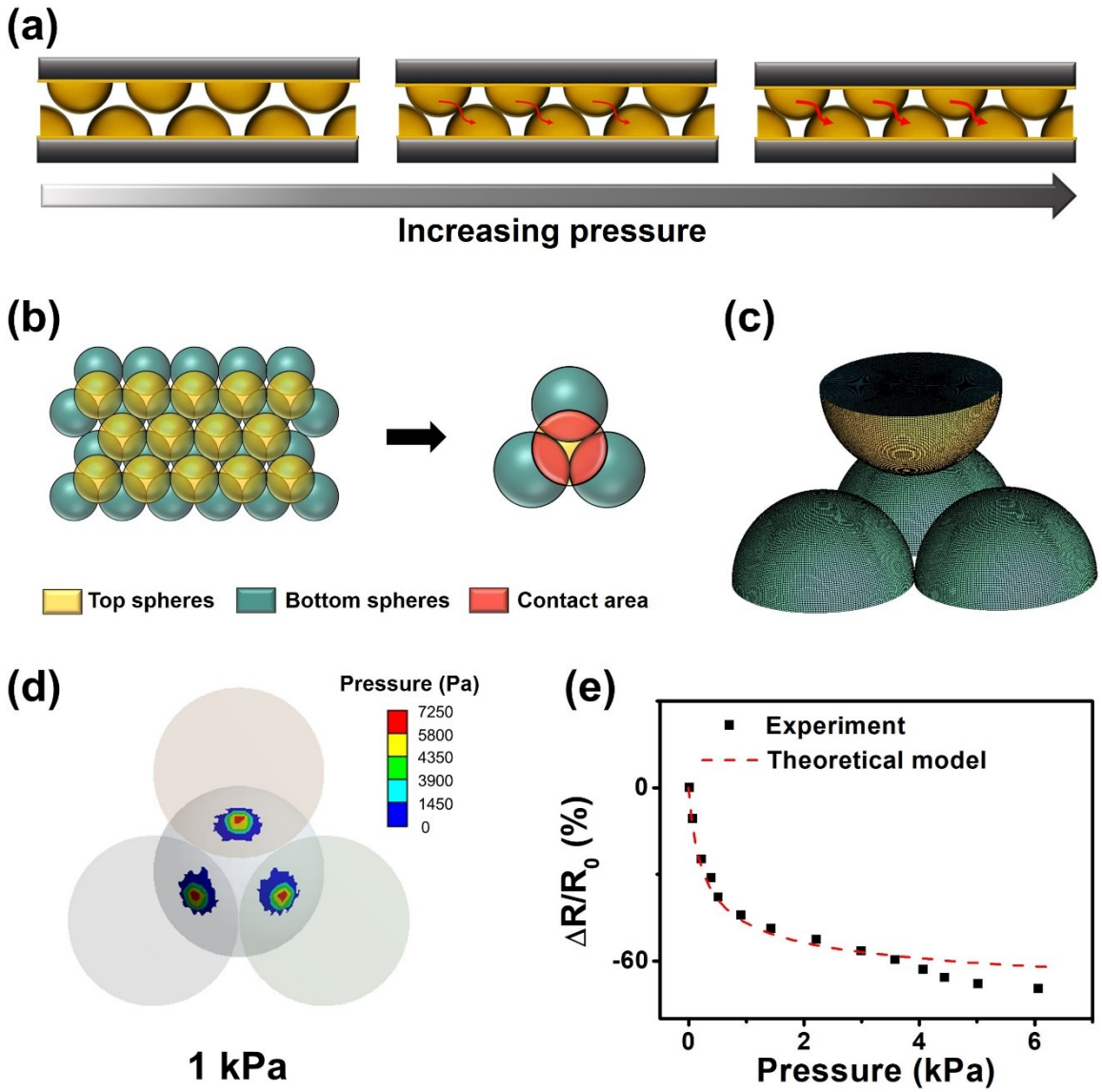

Figure S9. Sensing mechanism of the patterned Au/PDMS pressure sensor. (a) Schematics of the sensing mechanism of the pressure sensor with interlocked microdomes; (b) schematics of simplified contact area unit; (c) 3D model used in FEA; (d) contact pressure distribution of the interlocked microdomes under 1 kPa normal pressure; (e) comparison between the theoretical model and the experimental relative resistance changes of interlocked microdomes under pressure.

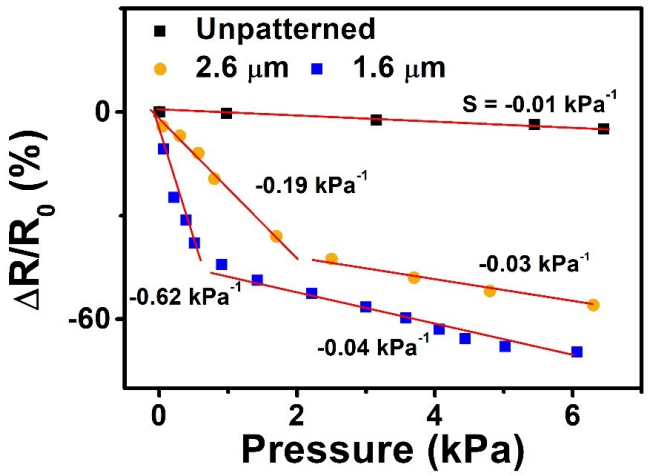

Figure S10. Piezoresistive behavior of the pressure sensor patterned using PS spheres of 1.6 and 2.6 μm in diameter.

The pressure sensors with interlocked microdome patterns showed much higher sensitivities than the unpatterned counterpart. The sensor patterned using PS spheres with a smaller size presented a higher pressure sensitivity (Figure S10), consistent with the previous findings.[38] Therefore, sensors fabricated from spheres with sizes of 1.6 μm were chosen for the integration of multidimensional sensors.

Sensing Mechanism of PUGA/PDMS Sensor

To unveil the underlying sensing mechanism of the in-plane sensor, the PUGA/PDMS composite was cryofractured and analyzed by SEM. As shown in Figure S11a, graphene flakes were interconnected in the PDMS matrix, constructing effective conductive pathways. Upon tensile loading, the separation of the initially interconnected flakes raised the resistance because of the increased tunneling distance.[28, 39] The strain simultaneously broke the conducting paths in the network, which also contributed to the exponential increase in resistance (Figure S11b). The numerous pre-cracks accounted for the significant resistance change and thus the enhanced

sensitivity of the PUGA/PDMS sensor compared to other sensing platforms described in Figure 5h and Table S1.

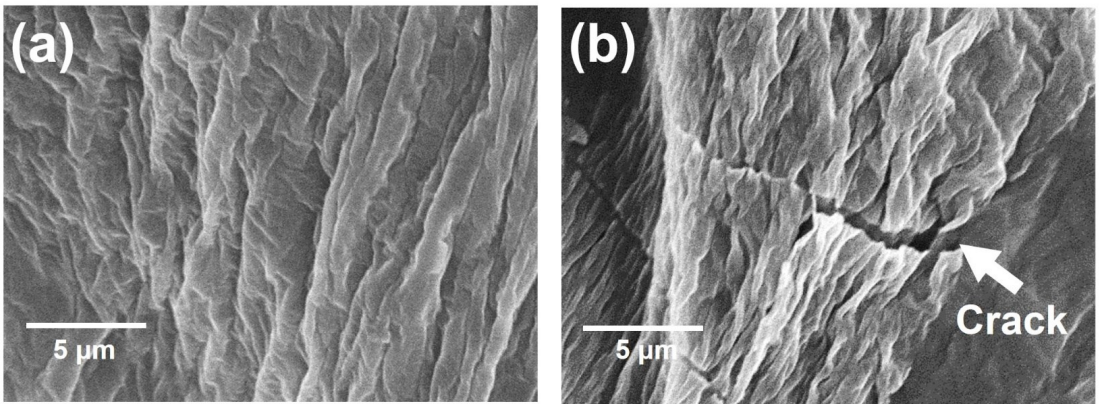

Figure S11. SEM images of PUGA composite under loading parallel to the alignment direction at (a) 0 % and (b) 10 % strain. Crack opening in the graphene skeleton can be clearly seen.

Tunneling Distance and Number of Conductive Paths in PUGA/PDMS Sensors

The resistance change in percolative composites is related to the change in the tunneling distance and number of conductive paths with increasing strain. The tunneling distance, w, increases with tensile strain, ε, according to the Equation S4:[28]

$$w = (1 + k\varepsilon)w_0 \quad \text{(S4)}$$

where k is a strain-independent parameter and w_0 is the initial tunneling distance without strain. The number of conductive paths, N, decreases with increasing strain as follows:[40]

$$N = \frac{N_0}{exp(A\varepsilon)} \quad \text{(S5)}$$

where A is a strain-independent parameter and N_0 is the initial number of conductive paths. k and A were determined by fitting Equation 2 with experimental data. The relative changes in tunneling distance and number of conductive paths when strains were applied in three different directions are shown in Table S2.

Table S2. Relative changes in tunneling distance and number of conductive paths at 25 % strains in different directions.

	Alignment	Transverse	Pressure
$(w- w_0)/w_0$	117 %	44 %	1 %
$(N- N_0)/N_0$	-80 %	~0	~0

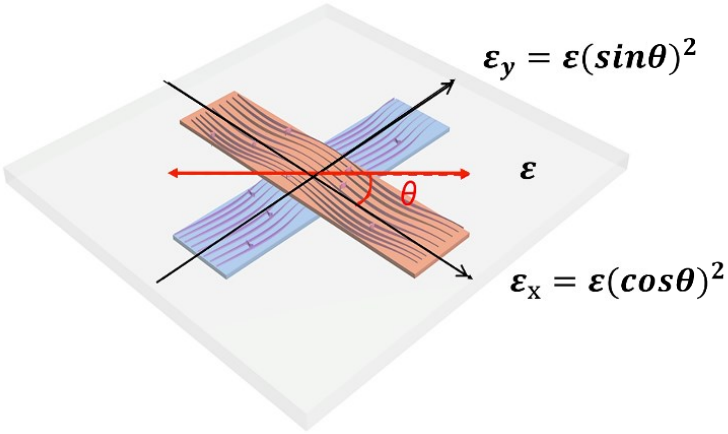

Figure S12. Schematic of the transformation of principal strains from one coordinate system to the other.

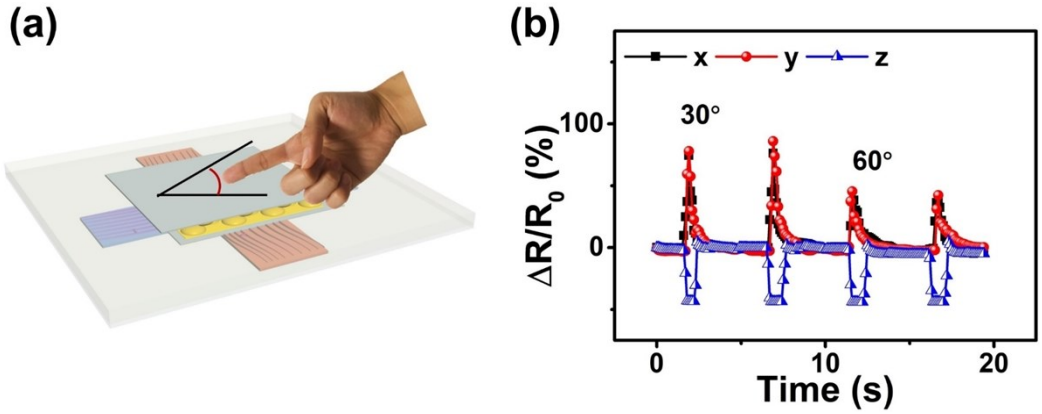

Figure S13. (a) Schematic showing the detection of a tilted force with an angle to the sensing plane; (b) relative resistance changes of the multidimensional sensor when a tilted force was applied at 30° and 60° to the sensing plane.

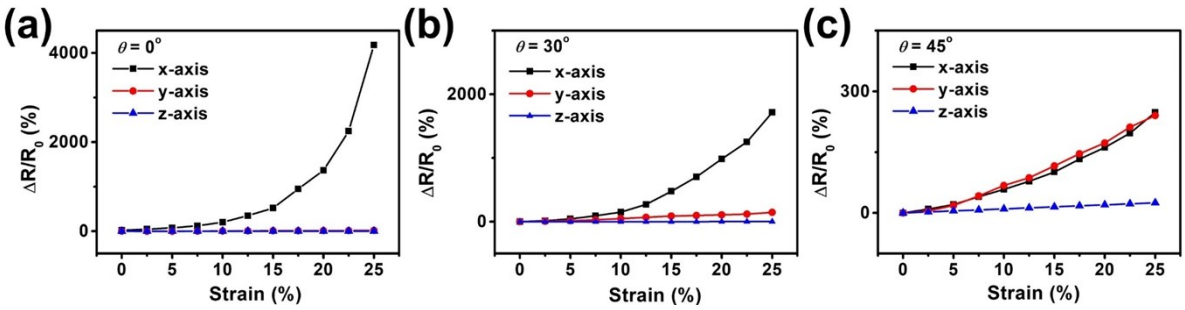

Figure S14. Relative resistance changes of the multidimensional sensor measured when a range of tensile strain 0 to 25 % was applied at different angles, θ, of (a) 0°, (b) 30°, and (c) 45° to the x-axis.

Table S3. Comparison between the actual and measured values of ε_1 and ε_2.

Actual values	**Measured θ**	**Measured magnitude**
ε_1 **(30°, 10 %)**	29.8°	10.4 %
ε_2 **(40°, 10 %)**	39.4°	10.5 %

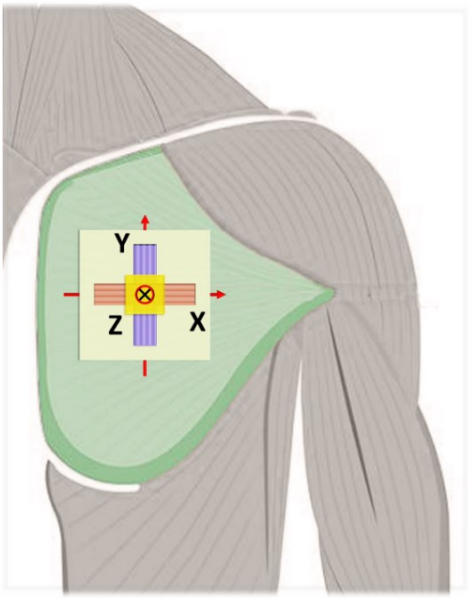

Figure S15. Schematic of sensor position attached to the chest for the smart sport assistant.

Video clips

Video_1: Real-time motion correction by the multidimensional sensor as a smart sport assistant.

Video_2: Danger alarming by the multidimensional sensor as a smart sport assistant.

References

1. S. H. Aboutalebi, M. M. Gudarzi, Q. B. Zheng and J.-K. Kim, *Adv. Funct. Mater.*, 2011, **21**, 2978-2988.
2. Q. Zheng, Z. Li, J. Yang and J.-K. Kim, *Prog. Mater Sci.*, 2014, **64**, 200-247.
3. Z. Wang, X. Shen, N. M. Han, X. Liu, Y. Wu, W. Ye and J.-K. Kim, *Chem. Mater.*, 2016, **28**, 6731-6741.
4. Z. Wang, N. M. Han, Y. Wu, X. Liu, X. Shen, Q. Zheng and J.-K. Kim, *Carbon*, 2017, **123**, 385-394.
5. N. M. Han, Z. Wang, X. Shen, Y. Wu, X. Liu, Q. Zheng, T.-H. Kim, J. Yang and J.-K. Kim, *ACS Appl. Mater. Interfaces*, 2018, **10**, 6580-6592.
6. Y. Wu, Z. Wang, X. Shen, X. Liu, N. M. Han, Q. Zheng, Y.-W. Mai and J.-K. Kim, *ACS Appl. Mater. Interfaces*, 2018, **10**, 26641-26652.
7. Q. Zheng, X. Liu, H. Xu, M.-S. Cheung, Y.-W. Choi, H.-C. Huang, H.-Y. Lei, X. Shen, Z. Wang, Y. Wu, S. Y. Kim and J.-K. Kim, *Nanoscale Horiz.*, 2018, **3**, 35-44.
8. J.-H. Lee, J. Kim, D. Liu, F. Guo, X. Shen, Q. Zheng, S. Jeon and J.-K. Kim, *Adv. Funct. Mater.*, 2019, **29**, 1901623.
9. Y. Hu, T. Zhao, P. Zhu, X. Liang, R. Sun and C.-P. Wong, *RSC Adv.*, 2015, **5**, 58-67.
10. L. Li, T. Zhai, H. Zeng, X. Fang, Y. Bando and D. Golberg, *J. Mater. Chem.*, 2011, **21**, 40-56.
11. S. H. Jeong, S. Zhang, K. Hjort, J. Hilborn and Z. Wu, *Adv. Mater.*, 2016, **28**, 5830-5836.
12. G. Yasin, M. Arif, M. Shakeel, Y. Dun, Y. Zuo, W. Q. Khan, Y. Tang, A. Khan and M. Nadeem, *Adv. Eng. Mater.*, 2018, **20**, 1701166.
13. X. Lin, X. Shen, Q. Zheng, N. Yousefi, L. Ye, Y.-W. Mai and J.-K. Kim, *ACS Nano*, 2012, **6**, 10708-10719.
14. M. Raisch, D. Genovese, N. Zaccheroni, S. B. Schmidt, M. L. Focarete, M. Sommer and C. Gualandi, *Adv. Mater.*, 2018, **30**, 1802813.
15. Z. Wu, S. Zhang, A. Vorobyev, K. Gamstedt, K. Wu, C. Guo and S. H. Jeong, *Mater. Today Phys.*, 2018, **4**, 28-35.
16. S. Wu, R. B. Ladani, J. Zhang, K. Ghorbani, X. Zhang, A. P. Mouritz, A. J. Kinloch and C. H. Wang, *ACS Appl. Mater. Interfaces*, 2016, **8**, 24853-24861.
17. X. Xie, Y. Zhou, H. Bi, K. Yin, S. Wan and L. Sun, *Sci. Rep.*, 2013, **3**, 2117.
18. F. Guo, X. Shen, J. Zhou, D. Liu, Q. Zheng, J. Yang, B. Jia, A. K. T. Lau and J.-K. Kim, *Adv. Funct. Mater.*, 2020, **30**, 1910826.
19. S. Ge, Z. Zhiheng, P. Jing‐Hong, L. Ivan, Z. Liqun, S. Craig, I. Kalana, Z. Rujing, Z. Hongwei and M. Jun, *Adv. Funct. Mater.*, 2016, **26**, 7614-7625.
20. Y. Lin, X. Dong, S. Liu, S. Chen, Y. Wei and L. Liu, *ACS Appl. Mater. Interfaces*, 2016, **8**, 24143-24151.
21. F. Pan, S.-M. Chen, Y. Li, Z. Tao, J. Ye, K. Ni, H. Yu, B. Xiang, Y. Ren, F. Qin, S.-H. Yu and Y. Zhu, *Adv. Funct. Mater.*, 2018, **28**, 1803221.
22. Z. Rujing, H. Ruirui, L. Xinming, Z. Zhen, X. Zhenhua, L. Na, H. Limin and Z.

Hongwei, *Adv. Funct. Mater.*, 2018, **28**, 1705879.
23. B. An, Y. Ma, W. Li, M. Su, F. Li and Y. Song, *Chem. Commun.*, 2016, **52**, 10948-10951.
24. D. Cho, J. Park, J. Kim, T. Kim, J. Kim, I. Park and S. Jeon, *ACS Appl. Mater. Interfaces*, 2017, **9**, 17369-17378.
25. C. Wang, Z.-Z. Pan, W. Lv, B. Liu, J. Wei, X. Lv, Y. Luo, H. Nishihara and Q.-H. Yang, *Small*, 2019, **15**, 1805363.
26. Z. Zeng, S. I. Seyed Shahabadi, B. Che, Y. Zhang, C. Zhao and X. Lu, *Nanoscale*, 2017, **9**, 17396-17404.
27. M. Amjadi, K.-U. Kyung, I. Park and M. Sitti, *Adv. Funct. Mater.*, 2016, **26**, 1678-1698.
28. X. Liu, D. Liu, J.-H. Lee, Q. Zheng, X. Du, X. Zhang, H. Xu, Z. Wang, Y. Wu, X. Shen, J. Cui, Y.-W. Mai and J.-K. Kim, *ACS Appl. Mater. Interfaces*, 2019, **11**, 2282-2294.
29. M. Amjadi, A. Pichitpajongkit, S. Lee, S. Ryu and I. Park, *ACS Nano*, 2014, **8**, 5154-5163.
30. H. Liu, Q. Li, Y. Bu, N. Zhang, C. Wang, C. Pan, L. Mi, Z. Guo, C. Liu and C. Shen, *Nano Energy*, 2019, **66**, 104143.
31. J. Lin, X. Cai, Z. Liu, N. Liu, M. Xie, B. Zhou, H. Wang and Z. Guo, *Adv. Funct. Mater.*, 2020, DOI: 10.1002/adfm.202000398.
32. J. Cui, B. Zhang, J. Duan, H. Guo and J. Tang, *Materials*, 2017, **10**, 1439.
33. R. S. Timsit, *IEEE Trans. Compon. Packaging Technol.*, 1999, **22**, 85-98.
34. R. Holm, *Electric contacts: theory and application*, Springer Science & Business Media, 2013.
35. J. Greenwood, *Br. J. Appl. Phys.*, 1966, **17**, 1621-1632.
36. N. Khalili, X. Shen and H. E. Naguib, *Soft Matter*, 2018, **14**, 6912-6920.
37. A. Chhetry, J. Kim, H. Yoon and J. Y. Park, *ACS Appl. Mater. Interfaces*, 2019, **11**, 3438-3449.
38. B. Zhu, Z. Niu, H. Wang, W. R. Leow, H. Wang, Y. Li, L. Zheng, J. Wei, F. Huo and X. Chen, *Small*, 2014, **10**, 3625-3631.
39. X. W. Zhang, Y. Pan, Q. Zheng and X. S. Yi, *J. Polym. Sci., Part B: Polym. Phys.*, 2000, **38**, 2739-2749.
40. L. Chen, G. Chen and L. Lu, *Adv. Funct. Mater.*, 2007, **17**, 898-904.